Results in Physics 29 (2021) 104679

Contents lists available at ScienceDirect

Results in Physics

journal homepage: www.elsevier.com/locate/rinp

Optical properties and surface dynamics analyses of homojunction and hetrojunction Q/ITO/ZnO/NZO and Q/ITO/ZnO/NiO thin films

Shahram Solaymani [a,*], Ştefan Ţălu [b], Negin Beryani Nezafat [c], Laya Dejam [d], Azizollah Shafiekhani [e], Atefeh Ghaderi [e], Amir Zelati [f]

[a] Department of Physics, Kermanshah Branch, Islamic Azad University, Kermanshah, Iran
[b] The Directorate of Research, Development and Innovation Management (DMCDI), Technical University of Cluj-Napoca, Constantin Daicoviciu St., no. 15, Cluj-Napoca 400020, Cluj County, Romania
[c] School of Physics, Institute for Research in Fundamental Sciences (IPM), P.O. Box 19395-5531, Tehran, Iran
[d] Department of Physics, West Tehran Branch, Islamic Azad University, Tehran, Iran
[e] Department of Physics, Faculty of Physics and Chemistry, Alzahra University, Tehran 1993891167, Iran
[f] Department of Basic Sciences, Birjand University of Technology, Birjand, Iran

ARTICLE INFO

Keywords:
Atomic force microscopy
Stereometric analysis
N/p ZnO transparent diodes
n-ZnO/p-NiO
n-ZnO/p-NZO

ABSTRACT

The aim of the present study is to verify how alternations of annealing temperatures modify optical and micromorphological properties of n-ZnO/p-NZO and n-ZnO/p-NiO multilayers. As can be seen, the optical analysis of homojunctions and hetrojunction thin films shows a red shift by increasing annealing temperature which means that annealing can shift absorption edge coefficient to the lower values of energies. Also, the effective parameters on optical properties of homo- and hetrojunction thin films such as optical band gap, Urbach energy, steepness parameter, and skin depth have been studied by their transmittance spectra. Moreover, the micromorphology of n/p ZnO homo- and heterojunctions transparent diodes have been studied by atomic force microscopy in combination with modern image processing techniques. The nano scaled stereometric analysis provides significant insights into the influence of preparation process on surface texture geometry. According to the results extracted from AFM micrographs by MountainsMap® software, it is observed that Q/ITO/ZnO/NZO sample with 300 °C annealing temperature has the normal distribution of peaks with the highest percentage of isotropy. In addition, it is observed that Q/ITO/ZnO/NiO with 500 °C annealing temperature has the most regular topography.

Introduction

As the next generation of wide-band gap semiconductors and optoelectronic instruments, transparent electronics has been motivated scientists in recent decade [1]. Transparent conductive oxides (TCOs) thin films are good candidate for optoelectronic devices and can transport electrical charge and visible photon due to their transparency, high flexibility, and lower voltage and power consumption and can be applied in flat panel displays such as plasma display panels, liquid crystal displays (LCDs), light-emitting-diodes (LEDs) [2], photovoltaics, and touch panels [3,4].

Both n- and p-type Zinc Oxide (ZnO) from II to VI semiconductor group are the most applicable materials that can be used in TCOs [5]. Doping ZnO with the group III (Al, Ga, and In) results in n-type ZnO [3–6]. As an ideal n-type transparent semiconductor, Ţălu et al. [7] studied the properties of ZnO thin films doped with aluminum (AZO) and investigated the effect of annealing temperatures on their surface morphology. They found that their topology and crystalline structures were enormously modified by post-annealing while the transparency was maximum in the AZO thin film annealed at 500 °C. On the other hand, Dalouji et al. [8] investigated the optical properties of AZO thin films and found that comparing to ZnO films, their band gap was wider. They also analyzed the effect of dopants on the microstructures and fractal features of Co-doped ZnO (Al and Cu and) thin films. Besides, Dejam et al. [9] showed that changing thickness would change CAZO and AZO thin films from semiconductor to conductor, but with more sensitivity in Co-doped layers and hence, they are useful candidate in electronic circuit switching. Li et al. [10] prepared sol–gel Al-doped ZnO

---

* Corresponding author.
E-mail address: shahram22s2000@yahoo.com (S. Solaymani).

https://doi.org/10.1016/j.rinp.2021.104679
Received 2 June 2021; Received in revised form 28 July 2021; Accepted 8 August 2021
Available online 20 August 2021

Table 1
Details of sputtering process for each sample.

Substrate	Labeled parameter	Base pressure (torr)	Working pressure (torr)	Power of sputtering (W)	Time of sputtering (min)	Sputtering gas	Thin film
Q		2×10^{-5}	6×10^{-3}	60	70	Ar	ITO
Q/ITO	#1 = S6	4×10^{-5}	6×10^{-3}	135	30	Ar	ZnO
Q/ITO/ZnO		2×10^{-5}	6×10^{-3}	135	40	Ar/N2	NZO
Q/ITO/ZnO		2×10^{-5}	6×10^{-3}	15	15	Ar/O2	NiO

Table 2
The annealing procedure of samples.

Sample	Labeled parameters	Annealing temperature (^{o}C)	Time of annealing (min)	Environment
Q/ITO/ZnO/NZO	#2 = S4	300	60	N2
Q/ITO/ZnO/NZO	#3 = S5	500	60	N2
Q/ITO/ZnO/NiO	#4 = S3	–	–	–
Q/ITO/ZnO/NiO	#5 = S2	300	60	N2
Q/ITO/ZnO/NiO	#6 = S1	500	60	N2

films. Although nanorod structures were initially found on the surface of pure ZnO, they gradually changed to nanosheets by increasing the concentration of doping. They also investigate the morphology of their prepared samples.

Native donor defects like oxygen vacancy (Vo) and zinc interstitial (Zni) along with low solubility of acceptor dopant is considerable in p-type doped ZnO [11]. The p-type ZnO is achieved by doping elements like P, NO, Cu, N2, and arsenic [12] whose unstable conduction even in room temperature converts it to n-type conduction easily [13]. Doping ZnO films with Copper (Cu) increases its c-axis preferred growth and electrical resistivity. Thus, Solaymani et al. [14] studied the influence of annealing treatments and Cu doping on the microstructure and photoluminescence of Cu-doped ZnO (CZO) thin films. Also, Pathak et al. [15] applied RF sputtering method for fabricating P-type ZnO thin films on n-type Si substrate and revealed their Hetrojunction behavior by I–V measurement. They approved significant application of p ZnO/n Si hetrojunction by investigating the effect of photon incident on their stability.

Nowadays, fabricating the oxide-based p–n junctions with high quality has attracted a lot of attentions in semiconductor technology where inserting dopants changes the metal oxide into p- or n-type conductions. Semiconductor junctions play an important role in the structure of basic transparent devices with transparent dielectric layers and electric contacts which is difficult to make [16].

Dejam et al. [17] studied the properties of the Cu2O/AZO heterojunction and achieved low turn-on voltage with the approximate value of 0.64 V which made them applicable in rectifier diode. They also calculated ideality factor as 10.28 and the PL emission peak from the p-n-junction was observed in 470 nm which was probably because of the existence of quantum-well at the junction in amorphous AZO. Finally, Finally, Shokri et al. [18] compared the electrical properties and the temperature-dependent resistivity of AZO/Au with theoretical results and demonstrated the exact compliancy of Au contact with tunneling current passing through the Schottky barrier at different temperatures.

In order to investigate optical parameters of homo and hetro junction thin films such as optical ban gap, Urbach energy, steepness parameter, and skin depth, their transmittance spectra have been analyzed.

On the other hand, visualizing surface micromorphology of thin films has a major role in the enhancement of their optical and physical properties which is possible by high-resolution images of atomic force microscopy (AFM) [19–21]. Thus, the simulation of surface topography can reveal 3-D surface microtexture and gives useful information through stereometric data containing motifs (peaks and pits) [22]. These motifs can be characterized by specific imaging methods like watershed segmentation algorithm while the stereometric data can be achieved by MountainsMap® Premium software.

In the present study, n/p ZnO homojunctions and heterojunctions transparent diodes have been synthesized at room temperature and different annealing temperature. As the next step, Optical properties of Transparent investigated and compared, also stability of junctions by annealing studied which has not been studied previously. On the other hand, we studied their 3-D surface texture using AFM data in connection with statistical and fractal analyses, to establish multiscale patterns of heterogeneous components for first time.

Experimental details

Thin films deposition

We were employed ZnO, ITO and NiO thin films for fabrication homojunctions and hetrojunctions on quartz substrates. The thin films were deposited by radio frequency (RF) sputtering techniques which was equipped with a multi-target system. Before the deposition, each quartz (Q) substrate was cleaned in ethylene and acetone in the ultrasonic bath for 15 min then were washed with deionized water.

As the first step, ITO thin films were deposited on quarts substrates by sputtering system. Secondly, ZnO/N:ZnO multilayer structure were deposited in a single deposition process without venting chamber. In order to grow ZnO thin films, Ar gas was inserted into sputtering chamber and ZnO was set as target. However, the working gas applied for growing N: ZnO (NZO) thin films were Ar (70%) and N_2 (30%). Therefore, we were able to make n-ZnO/p-NZO multilayer via above procedure. Details of deposition process for fabricating ZnO/NZO multilayer are given in Table 1.

Afterward, Ni and ZnO targets were used simultaneously to fabricate ZnO/NiO thin films with different working gas also without venting chamber. The only variable parameter was working gas so that Ar gas was used for ZnO thin film deposition and mix of Ar (70%) and O_2 (30%) gases was applied for growing NiO thin film. Therefore, we achieved n-ZnO/p-NiO multilayer structure. Details of their deposition process are summarized in Table 1.

Finally, we annealed both multilayers in N_2 environment for 1 h with

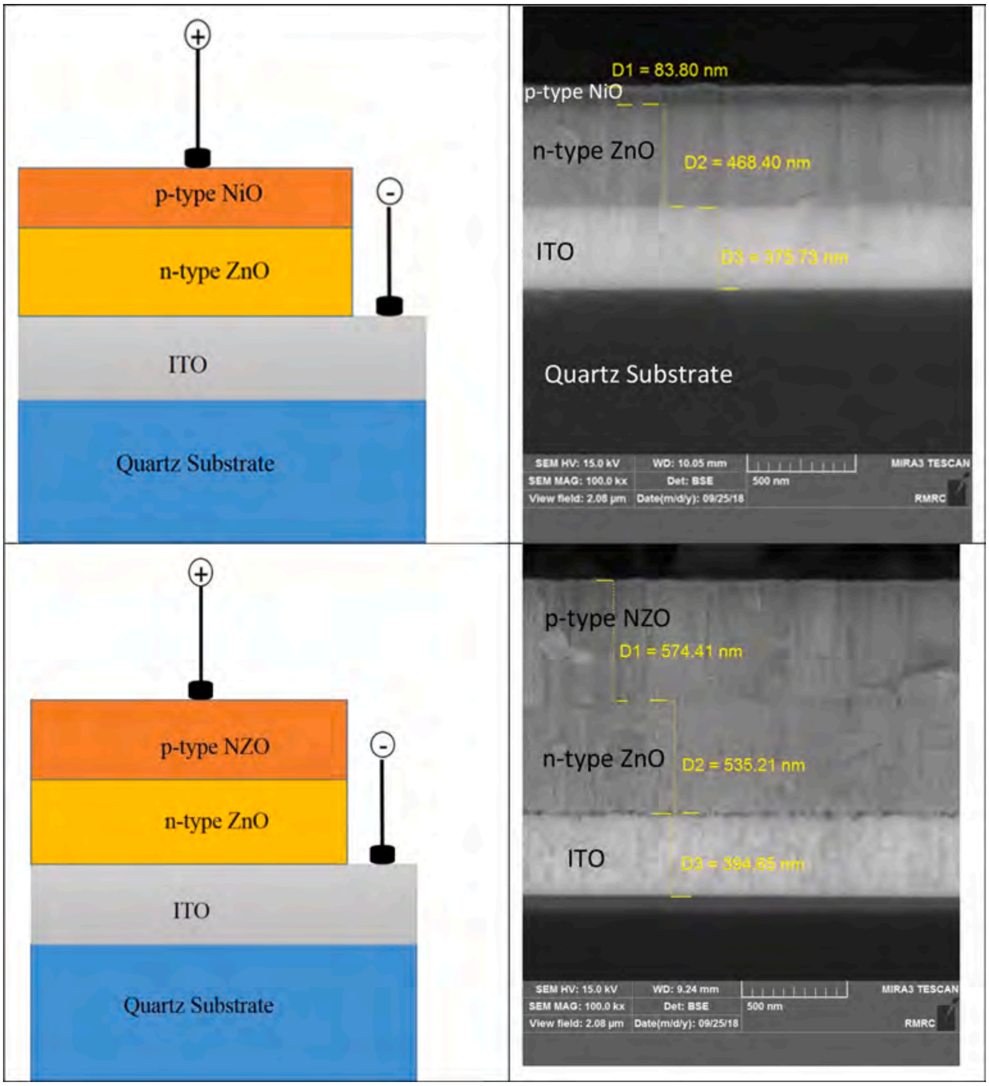

Fig. 1. The schematic of n/p ZnO homojunction and hetrojunction.

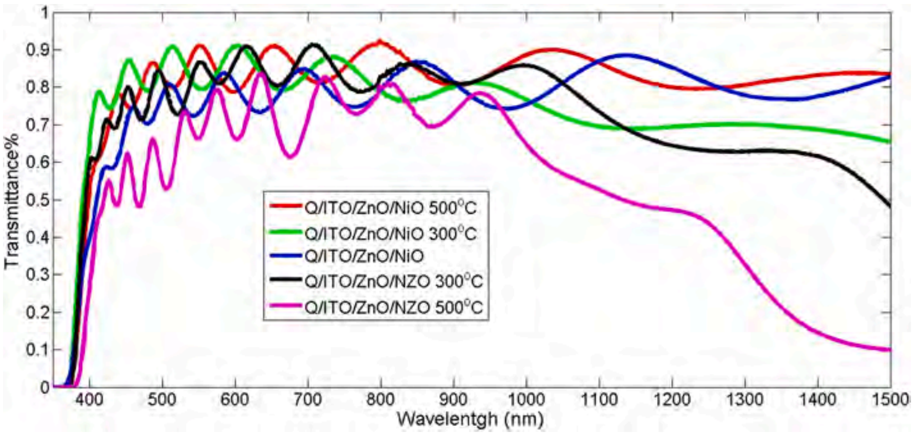

Fig 2. The diagram of transmittance vs. wavelength for as-deposited and annealed hetrojunction and homojunction thin films.

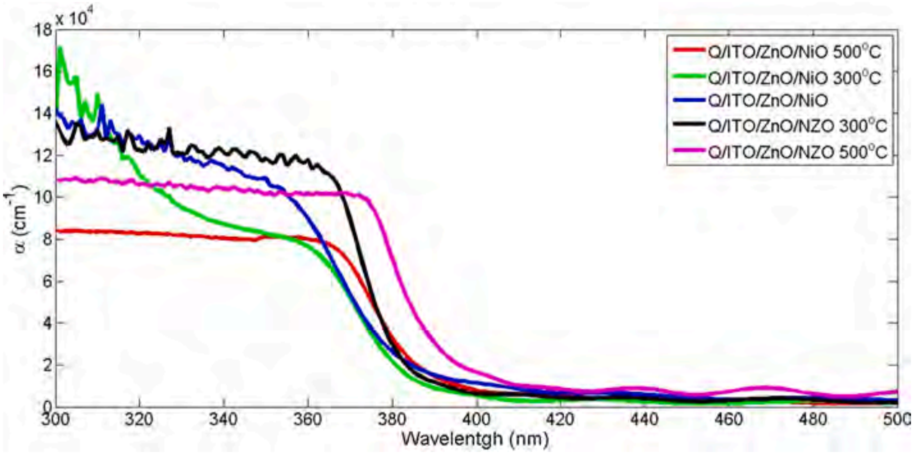

Fig 3. The absorption coefficient of as-deposited and annealed hetrojunction and homojunction thin films.

Table 3
The optical parameters of thin films.

Sample	E_g (eV)	E_u (eV)	Steepness parameters, σ	Electron–phonon interaction, $E_{e\text{-}p}$ (eV)
Q/ITO/ZnO/NiO	3.31	0.133	0.195	3.418
Q/ITO/ZnO/NiO 300 °C	3.29	0.095	0.270	2.469
Q/ITO/ZnO/NiO 500 °C	3.25	0.105	0.246	2.710
Q/ITO/ZnO/NZO 300 °C	3.29	0.075	0.342	1.949
Q/ITO/ZnO/NZO 500 °C	3.21	0.100	0.258	2.583

annealing temperatures of 300 and 500 °C which was done for stability of multilayers, especially NZO, since it converts to n-type conduction (Table 2). Applying the above procedure, we could fabricate ZnO homojunction and hetrojunction diode deposited on Q/ITO substrate. Fig. 1 represents the cross section of diode configuration.

Thin films and device characterization

The thickness of films was measured by a DEKTAK3 profilmeter. AFM measurements were conducted using AFM instrument Solver P47H-PRO (NT-MDT, Russia) in contact mode with single crystal N-type silicon probes VIT_P_C-A, 0.01–0.025 Ohm-cm, Antimony doped (Tips-Nano, Estonia) under ambient conditions (room temperature and relative humidity of about 50%). Standard images were acquired by a cantilever (with Al reflective coating, constant nominal force of 0.3 N/m, resonance frequency of 16 kHz, and a tip curvature radius of 6 nm) in 5 µm × 5 µm region with 512 × 512 pixels. Four images were acquired for each sample on random regions.

Results and discussion

Optical properties

The changes of transmittance spectra for both homo and hetrojunction thin films is illustrated in Fig. 2 where the percentage of average transmittance in the visible region is 80% approximately. As can

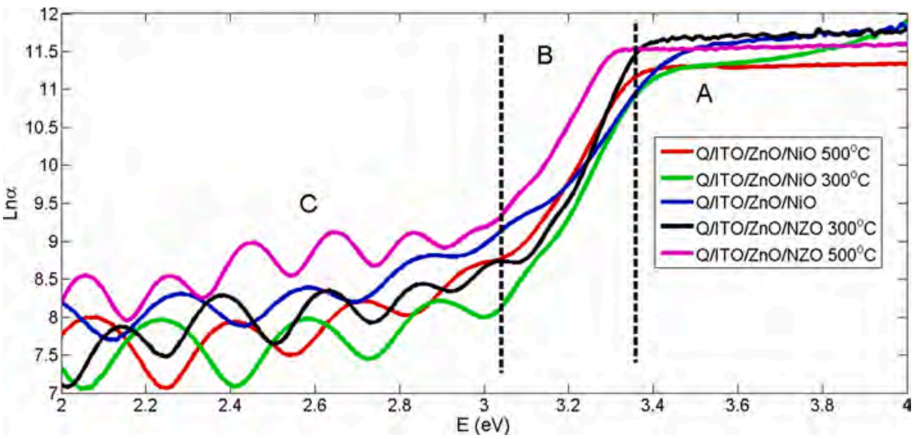

Fig.4. The diagram of Lnα as versus energy: hetrojunction and homojunction thin films.

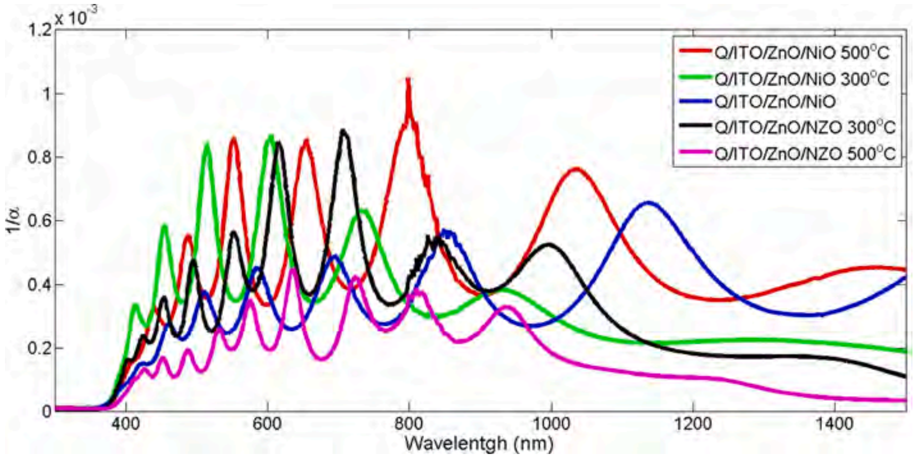

Fig.5. The skin depth variation: hetojunction and homojunction thin films.

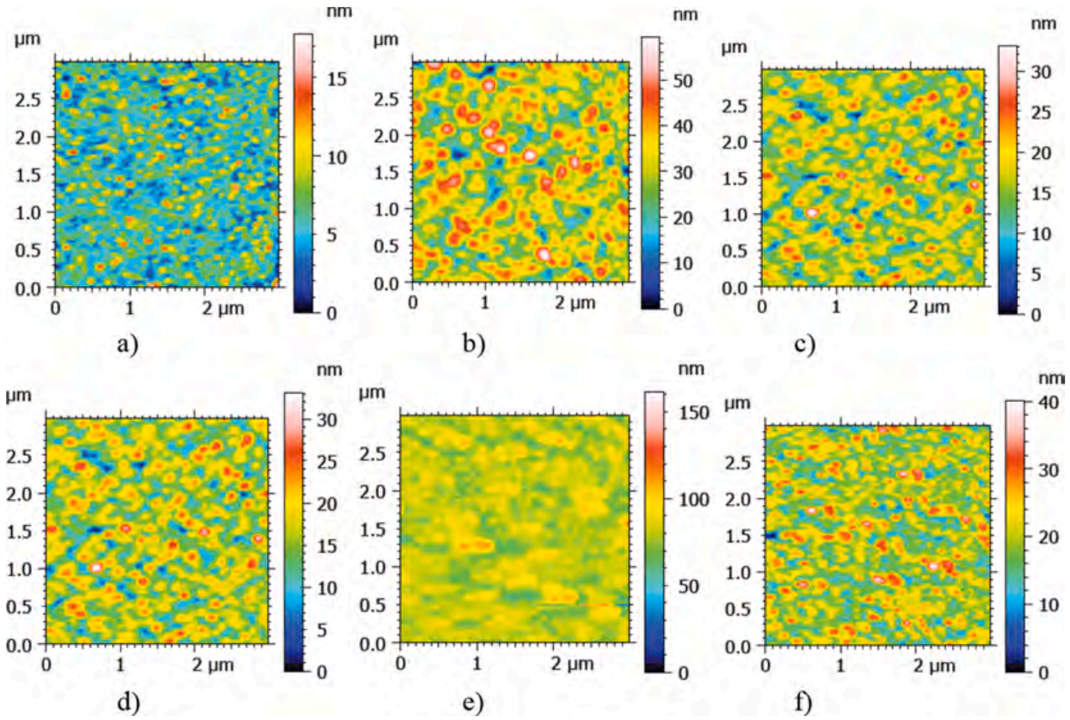

Fig. 6. Relevant 2-D AFM images of samples: a) #1, b) #2, c) #3, d) #4, e) #5, and f) #6.

be seen, the optical transmittance has been increased 90% after annealing process which makes them applicable in transparent thin film solar cell as a buffer layer [23].

Accordingly, the absorption coefficients can be calculated via α = 1/d Ln (1/T) where d is thickness. The relationship between α and photon energy is shown in Fig. 3 with a red shift by increasing annealing temperature which means that annealing could shift absorption edge coefficient to lower values of energies.

To determine optical band gap (E_g), Tauc's formula has been used based on relationship between photon energy and absorption coefficient (α) [24].

$$\alpha(\lambda)h\nu = A\left(h\nu - E_g\right)^m \tag{1}$$

where$A$ varies by transition probability. Here, hv is energy of photon and m is an index of optical absorption calculated as ½ and 2 for allowed direct and indirect transitions, respectively. The extrapolation of linear portion of curve to $(\alpha h\nu)^2 = 0$ is considered as the best way to calculate the optical band gap whose results are included in Table 3. It can be noted that optical band gap is decreased by increase of annealing temperature in both homo and hetrojunction thin films. Variations in layer structure and particles' size have strongly affected band gap. Funding shows that lowering the strain rate by annealing process and increasing the particle size can reduce band gap [25].

Some materials like disordered, low crystalized and amorphous ones show an exponential tail near optical band gap called Urbach tail where the localized states will be extended in band gap [25]. According to eq. (2), the absorption coefficient depends on photon energy under optical

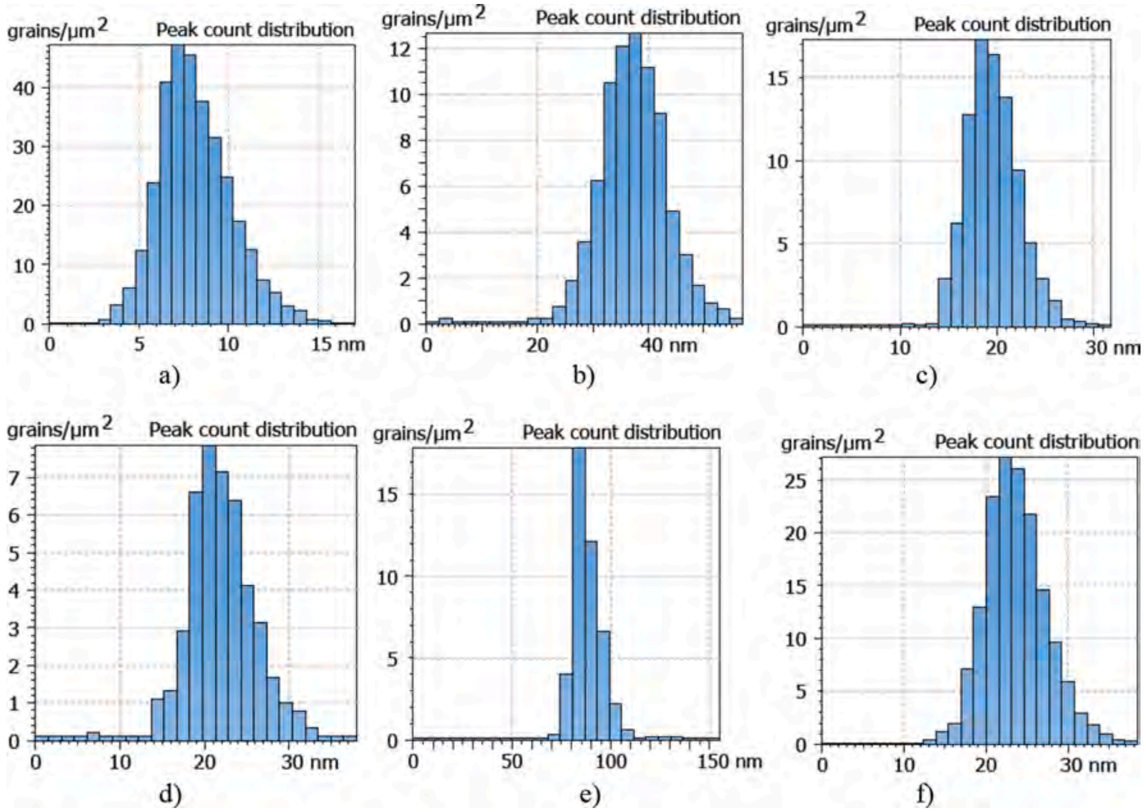

Fig. 7. The peak count histograms of samples: a) #1, b) #2, c) #3, d) #4, e) #5, and f) #6.

gap exponentially which means the tail absorption on photon energy.

$$\alpha(\lambda) \sim exp\left(\frac{h\nu}{E_u}\right) \tag{2}$$

whereE_u is the Urbach energy and it is achieved by calculating the slope of the diagram of Lnα versus photon energy as shown in Fig. 4. The results are presented in Table 3. It is obvious that the strong ionic bonds, lattice thermal vibrations, temperature, average photon energies, and induced and static disorders strongly affect Urbach energy. Therefore, E_u enhances with width of extended localized states which increase with annealing temperature.

σ is defined as the steepness parameter which specified the broadening of optical absorption edge appeared by exciton-phonon or electron–phonon interactions as below [26]:

$$\sigma = \frac{k_B T}{E_u} \tag{3}$$

Here, T and k_B are absolute temperature in Kelvin and Boltzmann constant, respectively. The following equation is applied for calculating the interaction strength of electron–phonon ($E_{e\text{-}p}$) [27]:

$$E_{e-p} = \frac{2}{3\sigma} \tag{4}$$

The results of Eqs. (3) and (4) are listed in table 3. It should be noticed that in both junction thin films, slow increase of annealing temperature narrows down the absorption edges. σ illustrates the shrinkage or broadening of exciton–phonon/electron–phonon interactions of optical absorption edges. Increasing E_u is related to localized states which are originated from the centers of non-radiative recombination, vacancies or dislocation defects in structure of films [28]. Here, the localized states strongly affect optical absorption response in forbidden band gap. Both disorder effects and localized states specified the forms of absorption edges.

Beside the ability of Urbach energy in calculating the width of localized states in amorphous films or nanocrystals around their optical bandgap, its exponential dependency to hυ which is originated from random variations of internal fields and structural disorders plays an important role [29]. Moss–Burstein effect supports the fact that increasing annealing temperature decreases bandgap and increases carrier concentration [30].

Thickness, extinction coefficient, and photo-conductivity have significant influence on the absorption of electromagnetic wave in thin films. On the other hand, refractive index, density, photon current density, and microstructure of films are decreased by moving from the surface to inside of sample exponentially which is confirmed by surface morphology.

The depth where in proportion of radiation intensity inside medium to radiation intensity on surface becomes 1/e (about 37%) is called Skin depth χ and is calculated by following equation [31]:

$$\chi = \frac{1}{\alpha} \tag{5}$$

Here, α is absorption coefficient. As can be seen in Fig. 5, the energy of incident photon strongly affects χ in hetro and homojunctions annealed films. As can be seen, while the skin depth of hetrojunctions

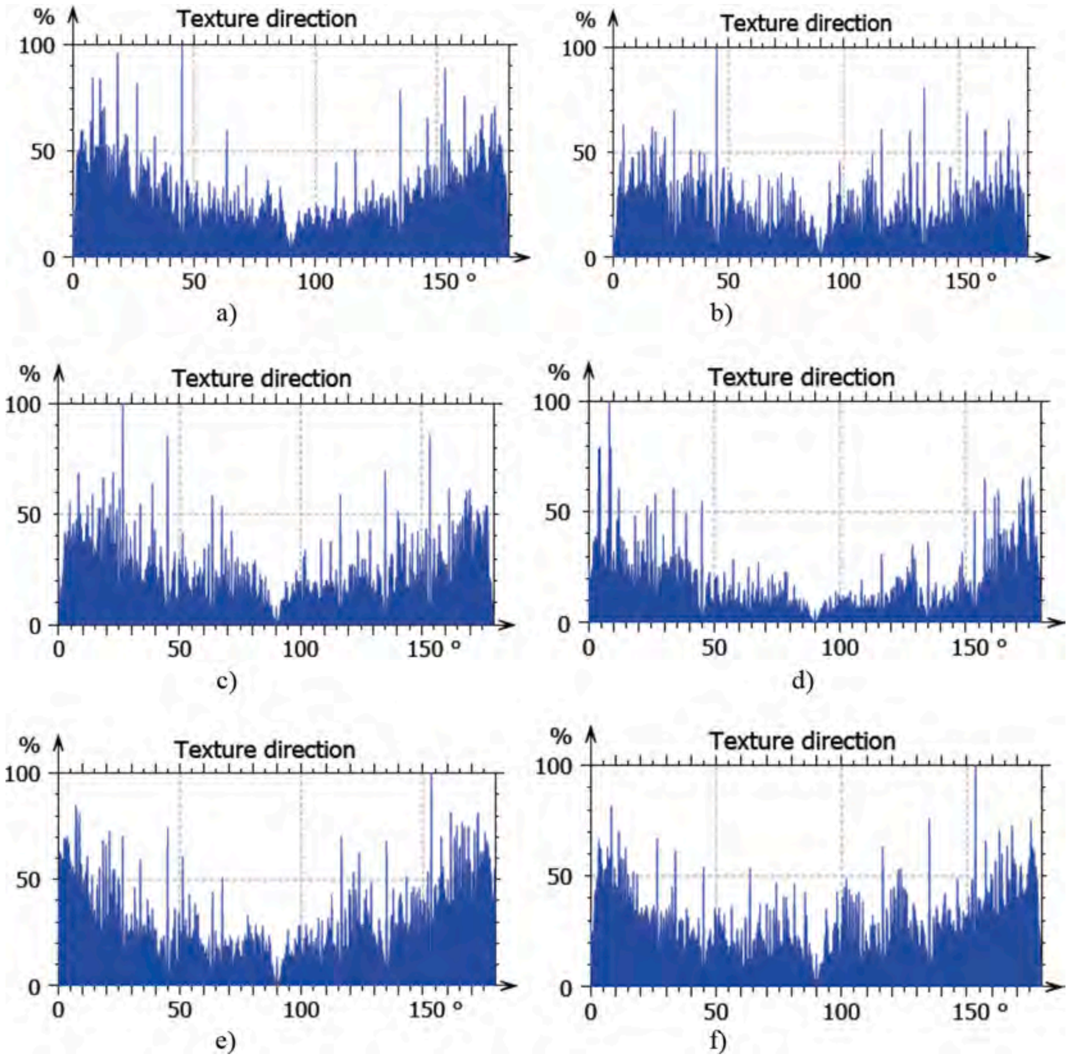

Fig. 8. The graphical study of surface texture directions in Cartesian graphs for: a) #1, b) #2, c) #3, d) #4, e) #5, and f) #6.

Table 4
The computed values of surface texture directions.

Parameters	#1	#2	#3	#4	#5	#6
Isotropy [%]	67.55	81.39	73.83	69.80	52.61	65.96
First direction [°]	44.99	45.01	26.47	8.295	153.6	153.6
Second direction [°]	18.53	135.0	153.5	175.6	7.258	8.219
Third direction [°]	153.5	26.46	45.00	157.5	161.5	135.0

increased by increasing annealing temperatures, an inverse behavior is observed in homojunction thin films which is considered to happen due to presence of NiO thin film instead of ZnO thin film.

Stereometric analysis of 3-D nanostructures

The software OriginPro 2016 (OriginLab, MA, USA) was applied for statistical analysis. Variance analysis (ANOVA) was employed using a p-value of 0.05 ($p < 0.05$).

AFM, in combination with modern image processing techniques, offers advanced facilities for extracting particular topographic features of surfaces and highlights the local nanoscale configuration of 3-D complex surfaces [32–35]. The microtexture of the 3-D surface can be quantified by stereometric [36–39] and fractal [40–42] and multifractal [43,44] methods.

Surface topography was evaluated using AFM topographic maps with MountainsMap® Premium software ver. 8.2 [45] in accordance to ISO 25178–2: 2012 standard [46].

The representative AFM 2-D images of the analyzed samples, for scanning the 3 μm × 3 μm square surfaces, are shown in Fig. 6. The images reveal a various 3-D micromorphology with specific height probability distributions for different roughness sizes.

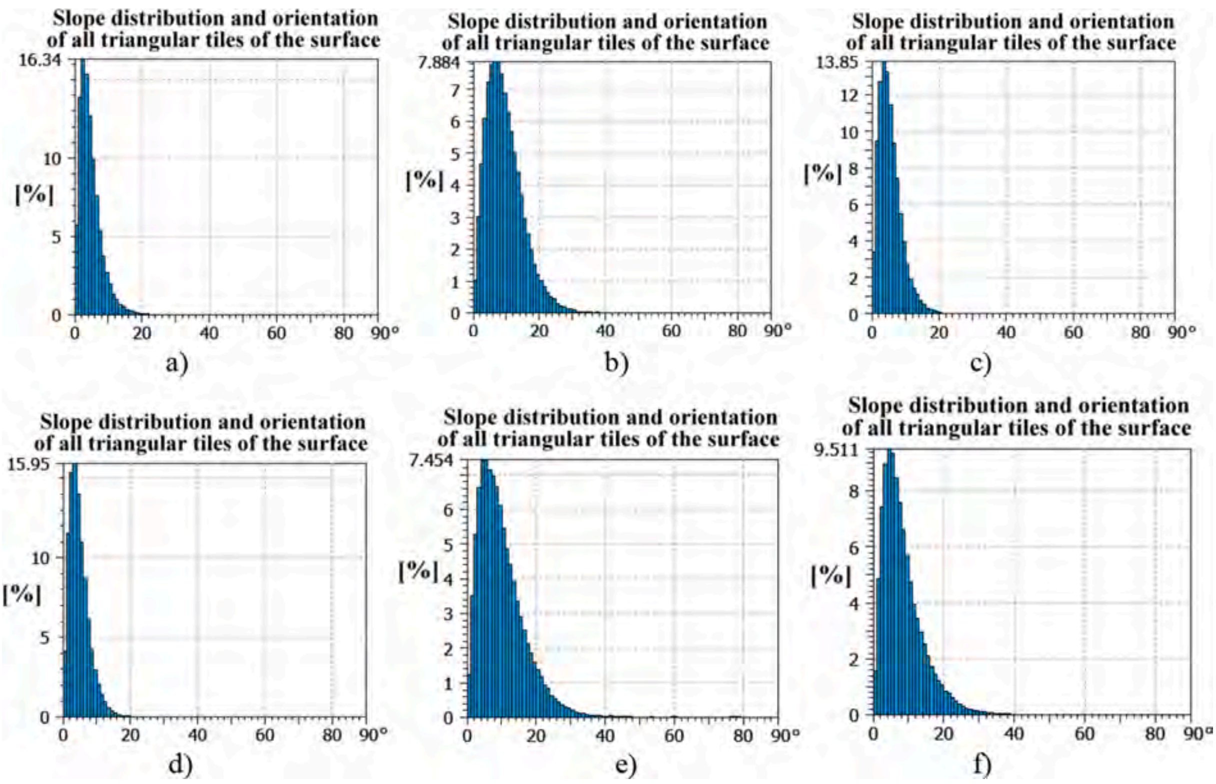

Fig. 9. The distribution of slope and orientation of all triangular tiles composing the surface for: a) #1, b) #2, c) #3, d) #4, e) #5, and f) #6.

Table 5
The computed parameters of slope and orientation of all triangular tiles composing the surface.

Parameters	#1	#2	#3	#4	#5	#6
Circular mean [°]	4.616	9.465	5.430	4.774	10.17	8.351
Mean resultant length	0.9985	0.9954	0.9982	0.9987	0.9916	0.9950
Main [°]	2.286	6.265	3.704	3.268	5.735	4.407

Fig. 7 shows the peak count histograms associated with relevant analysed samples from Fig. 6. It is highlighted that histograms associated with groups (#2 and #6) have a normal distribution, whereas all other histograms have a right-skewed distribution.

The graphical study of surface texture directions in Cartesian graphs is given in Fig. 8 and the results were summarized in Table 4.

The obtained results of surface texture directions in Cartesian graphs from Fig. 8 are summarized in Table 4.

The highest value for isotropy was found for sample #2 (81.39), whereas the lowest value (52.61) is associated with sample #5. Also, sample #5 has the highest values for parameters: first direction (153.6°), third direction (161.5°), and the lowest value for the second direction (7.258°). For the second direction the highest value was found for sample #4 (175.6°).

The distribution of slope and orientation of all triangular tiles composing the surface (using the normal vector of each tile used as a reference) of analyzed samples are graphical represented in Fig. 9 and the computed values are summarized in Table 5.

All histograms associated with distribution of slope and orientation of all triangular tiles composing the surface have a right-skewed distribution. The highest value for the circular mean parameter was found for sample #5 (10.17°), whereas the lowest value (4.774) is associated with sample #4. Both these values are well correlated with the first direction parameter of samples. In addition, the mean resultant length parameter has a value of about 0.99 for all samples. The parameter main has the highest value for sample #2 (6.265°), whereas the lowest value is associated with sample #1 (2.286°).

The graphical images of the step height calculations is illustrated in Fig. 10 and the computed results are summarized in Table 6.

The graphical representation of the step height calculations reveal various height differences of the surface samples relative with the plane parameters. The highest values of all parameters correspond for sample #5, while the lowest values are found with sample #1.

The fractal dimension with coefficients of correlation (R^2), obtained by the enclosed volume method [43], are graphical illustrated in Fig. 11 and the computed results are summarized in Table 7. The coefficients of correlation (R^2) of all linear fits for all groups were more than 0.992 ± 0.001.

The fractal dimension of sample #1 has the highest value ($Df = 2.75 \pm 0.01$, the higher irregular topography), and the lowest value belongs

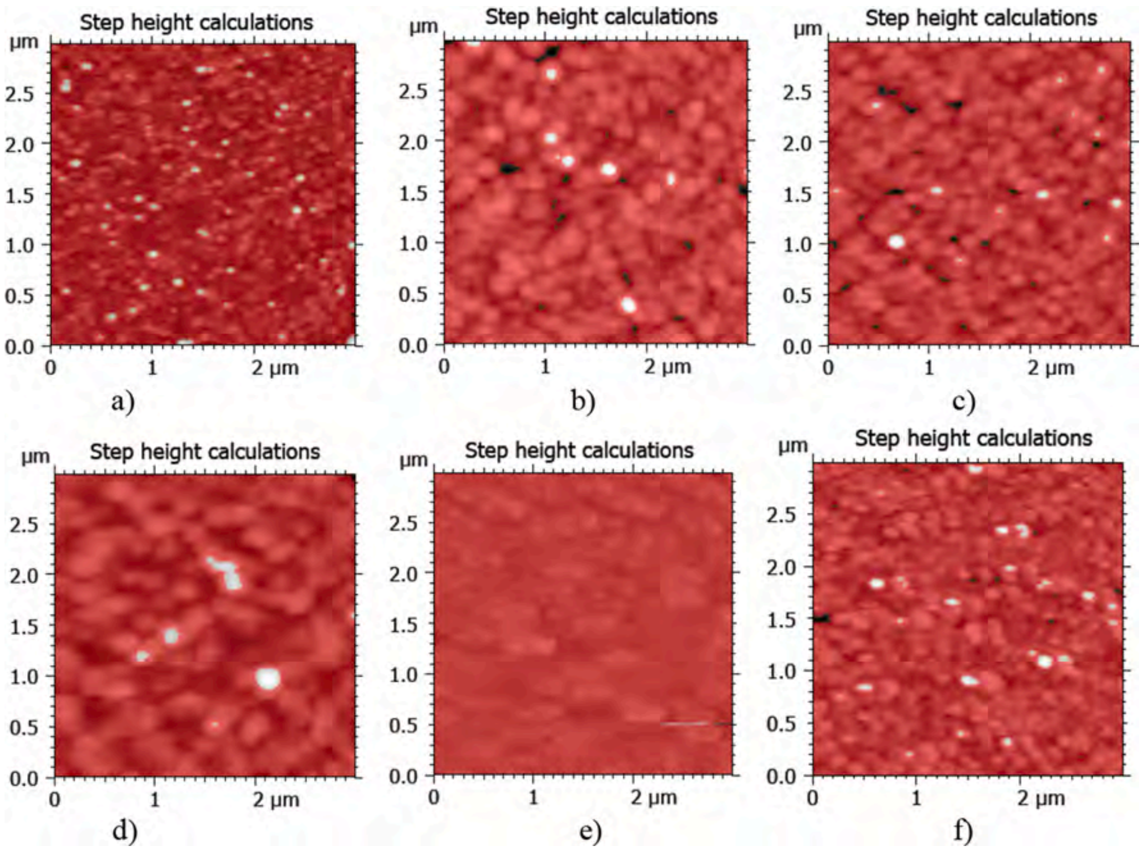

Fig. 10. The graphical images of step height calculations distribution for: a) #1, b) #2, c) #3, d) #4, e) #5, and f) #6.

Table 6
The plane parameters of step height calculations of samples.

Plane parameters	#1	#2	#3	#4	#5	#6
Z_{min} [nm]	0.5	12.4	6.6	3.0	53.8	8.4
Z_{mean} [nm]	6.2	31.6	16.2	17.3	81.6	19.8
Z_{max} [nm]	12.0	51.6	26.4	30.8	114.9	32.0

to sample #5 (*Df* = 2.43 ± 0.01, the most regular topography).

The graphical images of the frequency spectrum is shown in Fig. 12 and the computed values of analyzed samples are summarized in Table 8.

The graphs of frequency spectrum confirm the topographical changes in surface texture. The magnitude of sample #1 has the lowest value (−76.58), while the highest value is associated with sample #3 (−67.62).

The results of the statistical surface parameters based on ISO 25178-2: 2012 standard is illustrated in Tables 9 and 10.

The highest root mean height (Sq), is associated with samples #2 and sample #5 (8.0 ± 0.1 nm), whereas the lowest one has the sample #1 (2.1 ± 0.1 nm). The Ssk parameter of all samples is positive (that indicates surfaces with peaks), except sample #3 which is negative (that indicates a predominance of valleys). The highest value of Ssk appears in sample #1 (0.83 ± 0.01), while the lowest one in the sample #3 (−0.02 ± 0.01). The surface kurtosis (Sku) qualify the flatness of the height distribution. It can be seen that all samples are spiky surfaces.

The areal material ratio parameter has the same value for all samples (Smr = 100). The highest values for the parameters: Sal (0.1047 µm), and Sdr (1.898 %) were found for sample #2; while lowest values for the parameters: Sal (0.1047 µm) is found in sample #5, and Sdr (0.4852 %) were found for sample #1. The functional parameters (volume): Vm, Vv, Vmp, and Vvc have the highest values for sample #5, and the lowest values are associated with sample #1. The parameters Vmc, and Vvv have the highest values for sample #2, and the lowest values are associated with sample #1.

The feature parameter Spd has the highest value for sample #1 (49.05 [1/µm^2]), whereas the lowest value is associated with sample #4 (8.511 [1/µm^2]). The other parameters: Spc, S10 z, S5p, S5v, Sda, Sha, Sdv, and Shv have the highest values for sample #5. S5p, S5v, Sda, and Sha parameters have the lowest values for sample #1, and Sdv, and Shv have the lowest values for sample #6.

The Stratified surfaces: Sk, Spk, and Svk have the lowest values for sample #1; while Sk, and Svk have the highest values for sample #2, and Spk for sample #5. In opposite, the highest values for parameters Smrk1 and Smrk2 are associated with sample #1; while Smrk1 has the lowest value for sample #2, and Smrk2 for sample #5.

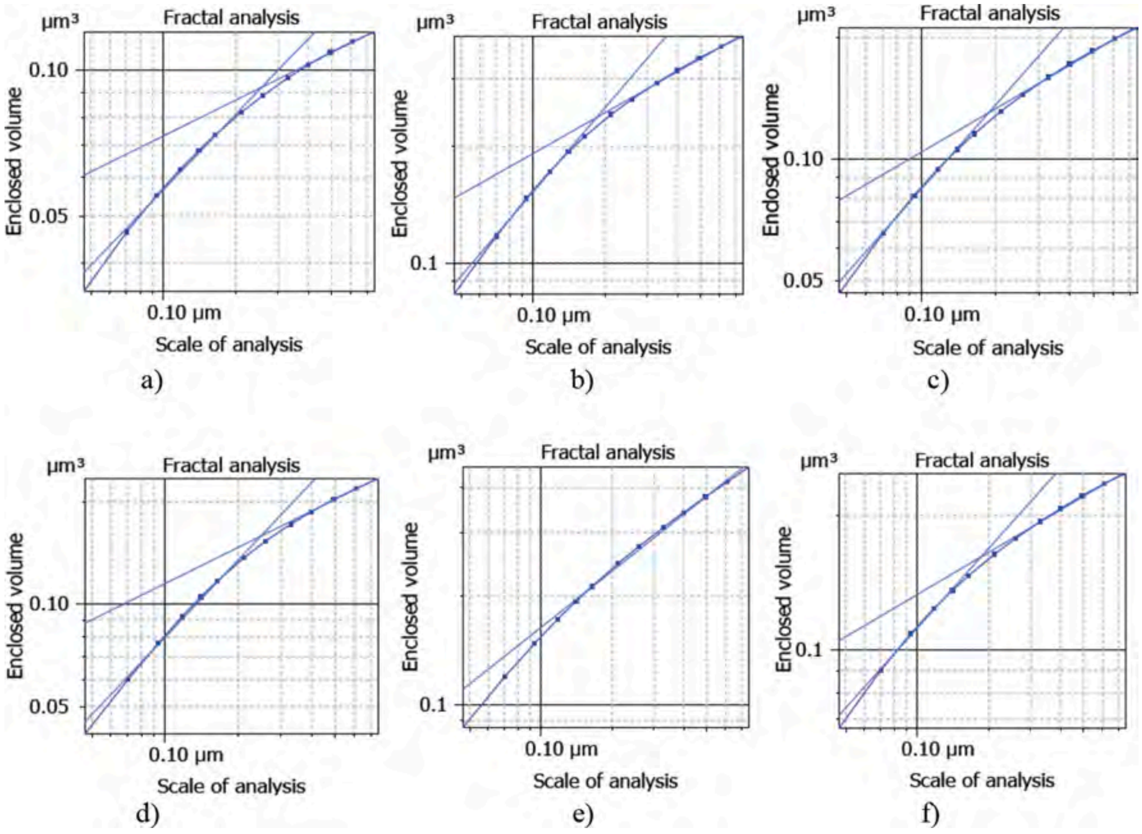

Fig. 11. The graphs of the enclosed volume method for determination of fractal dimension for: a) #1, b) #2, c) #3, d) #4, e) #5, and f) #6.

Table 7
The fractal dimensions (*Df*) for analyzed samples expressed as mean value and standard deviation.

Fractal dimension	#1	#2	#3	#4	#5	#6
Df	2.75 ± 0.01	2.51 ± 0.01	2.61 ± 0.01	2.71 ± 0.01	2.43 ± 0.01	2.59 ± 0.01

* Statistically significant difference: $P < 0.05$.

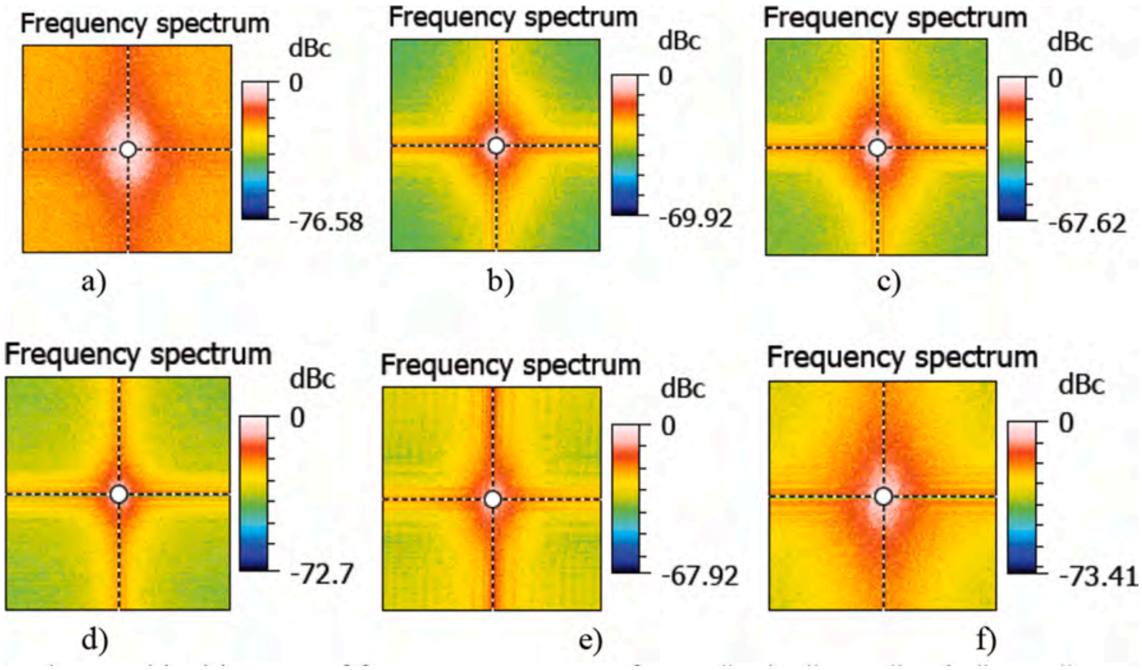

Fig. 12. The graphical images of frequency spectrum for: a) #1, b) #2, c) #3, d) #4, e) #5, and f) #6.

Table 8
The computed parameters for the frequency spectrum of analyzed samples.

Parameter	#1	#2	#3	#4	#5	#6
Magnitude [dBc]	−76.58	−69.92	−67.62	−72.7	−67.92	−73.41

Table 9
The statistical parameters for the analyzed samples: a) #1, b) #2, and c) #3, are according with ISO 25178–2: 2012.

The statistical parameters	Symbol	# 1 Values	# 2 Values	# 3 Values
Height parameters				
Root mean square height	Sq [nm]	2.1	8.0	3.9
Skewness	Ssk [–]	0.83	0.00	−0.02
Kurtosis	Sku [–]	4.12	3.09	3.25
Functional parameters				
Areal material ratio	Smr [%]	100	100	100
Spatial parameters				
Auto-correlation length	Sal [μm]	0.0527	0.1047	0.07951
Texture-aspect ratio	Str [–]	0.6755	0.8139	0.7383
Hybrid parameters				
Root mean square gradient	Sdq [–]	0.09894	0.1972	0.1134
Developed interfacial area ratio	Sdr [%]	0.4852	1.898	0.6364
Functional parameters (volume)				
Material volume	Vm [μm^3/μm^2]	0.000154	0.000394	0.000185
Void volume	Vv [μm^3/μm^2]	0.003025	0.01063	0.005144
Peak material volume	Vmp [μm^3/μm^2]	0.000154	0.000394	0.000185
Core material volume	Vmc [μm^3/μm^2]	0.001735	0.007289	0.003506
Core void volume	Vvc [μm^3/μm^2]	0.002858	0.009756	0.004692
Pit void volume	Vvv [μm^3/μm^2]	0.000167	0.00873	0.000451
Feature parameters				
Density of peaks	Spd [1/μm^2]	49.05	15.68	19.26
Arithmetic mean peak curvature	Spc [1/μm]	9.143	4.314	3.534
Ten point height	S10z [nm]	16.38	55.24	29.03
Five point peak height	S5p [nm]	10.23	25.65	13.72
Five point pit height	S5v [nm]	6.148	29.59	15.32
Mean dale area	Sda [μm^2]	0.02954	0.07409	0.06828
Mean hill area	Sha [μm^2]	0.02094	0.06894	0.05369
Mean dale volume	Sdv [μm^3]	4.63e-06	4.50e-05	2.55e-05
Mean hill volume	Shv [μm^3]	8.45e-06	11.5e-05	3.55e-05
Functional parameters (Stratified surfaces)				
Core roughness depth	Sk [nm]	4.642	21.34	10.03
Reduced summit height	Spk [nm]	3.302	7.792	3.719
Reduced valley depth	Svk [nm]	1.354	7.468	3.929
Areal material ratio of the scale-limited surface	Smrk1 [%]	15.82	9.183	9.518
Areal material ratio of the scale-limited surface	Smrk2 [%]	92.50	91.17	89.93

* Statistically significant difference: $P < 0.05$.

Table 10
The statistical parameters for the analyzed samples: a) #4, b) #5, and c) #6, are according with ISO 25178–2: 2012.

The statistical parameters	Symbol	# 4 Values	# 5 Values	# 6 Values
Height parameters				
Root mean square height	Sq [nm]	5.3	8.0	4.7
Skewness	Ssk [–]	0.27	0.38	0.39
Kurtosis	Sku [–]	3.22	6.60	3.37
Functional parameters				
Areal material ratio	Smr [%]	100	100	100
Spatial parameters				
Auto-correlation length	Sal [μm]	0.1273	0.09857	0.0681
Texture-aspect ratio	Str [–]	0.6980	0.5261	0.6596
Texture direction	Std [°]	176.3	2.752	176
Hybrid parameters				
Root mean square gradient	Sdq [–]	0.09894	0.3098	0.1836
Developed interfacial area ratio	Sdr [%]	0.4856	3.176	1.640
Functional parameters (volume)				
Material volume	Vm [μm^3/μm^2]	0.000298	0.000517	0.000282
Void volume	Vv [μm^3/μm^2]	0.007107	0.01067	0.00652
Peak material volume	Vmp [μm^3/μm^2]	0.000298	0.000517	0.000282
Core material volume	Vmc [μm^3/μm^2]	0.004849	0.006628	0.004133
Core void volume	Vvc [μm^3/μm^2]	0.006588	0.009836	0.006084
Pit void volume	Vvv [μm^3/μm^2]	0.000518	0.008311	0.000435
Feature parameters				
Density of peaks	Spd [1/μm^2]	8.511	10.53	31.80
Arithmetic mean peak curvature	Spc [1/μm]	3.532	28.69	8.266
Ten point height	S10z [nm]	32.04	83.04	33.63
Five point peak height	S5p [nm]	17.37	46.63	18.40
Five point pit height	S5v [nm]	14.68	36.41	15.23
Mean dale area	Sda [μm^2]	0.1529	0.2724	0.03526
Mean hill area	Sha [μm^2]	0.1334	0.09766	0.03363
Mean dale volume	Sdv [μm^3]	6.41e-05	26.3e-05	1.09e-05
Mean hill volume	Shv [μm^3]	14.4e-05	16.1e-05	3.40e-05
Functional parameters (Stratified surfaces)				
Core roughness depth	Sk [nm]	13.83	17.96	11.62
Reduced summit height	Spk [nm]	5.966	10.65	5.856
Reduced valley depth	Svk [nm]	4.256	7.249	3.468
Areal material ratio of the scale-limited surface	Smrk1 [%]	10.08	13.23	12.58
Areal material ratio of the scale-limited surface	Smrk2 [%]	91.38	89.70	91.89

* Statistically significant difference: $P < 0.05$.

Conclusions

The present work was mainly focused applying Zinc Oxide, Indium tin oxide and Nickel oxide thin films for fabricating n/p ZnO homojunction and hetrojunction diodes. n-ZnO/p-NZO and n-ZnO/p-NiO multi layers were deposited by radio frequency sputtering techniques and effect of annealing temperature on their surface micromorphology also optical properties were studied. A red shift in optical analysis of homo and hetrojunction thin films by increasing annealing temperature demonstrated that the annealing could shift absorption edge coefficient to lower energies. Moreover, increasing annealing temperature increased the skin depth of hetrojunctions in decreased skin depth of homojunction thin films whose reason was the presence of NiO and ZnO thin film in those thin films. Also, the enhancement of Urbach energy with the width of extended localized states and annealing temperature was demonstrated.

Furthermore, stereometric analyses achieved valuable information about micrographs of AFM images. The 3-D surface microtexture of samples enhanced certainty in modeling the surfaces. Therefore, the 3-D surface microtexture was a central point for understanding surface topography which was applied as a means for computer simulation and accurate mathematical models. Applying MountainsMap® software indicated that for Q/ITO/ZnO/NZO, increasing annealing temperature decreased the isotropy. Although increasing annealing temperature from 25 °C to 300 °C decreased the isotropy in Q/ITO/ZnO/NiO, it was increased as the temperature changed form 300 °C to 500 °C. Moreover the most regular sample with lowest fractal dimension was achieved in Q/ITO/ZnO/NiO sample with 500 °C annealing temperature and the substrate itself had the lowest topographical changes, maximum fractal dimension and hence, the lowest topography. Finally, surface kurtosis (Sku) parameter indicated the flatness of height distribution where all samples had spiky surfaces.

The data availability statement

The data that support the findings of this study are available from the corresponding author upon reasonable request.

Declaration of Competing Interest

The authors declare that they have no known competing financial interests or personal relationships that could have appeared to influence the work reported in this paper.

References

[1] Lu Y, Warner JH. ACS Appl Electron Mater 2020;2(7):1777–814.
[2] Song J, He Y, Chen J, Zhu D, Pan Z, Zhang Y, et al. J Elec Materi 2012;41:431–6.
[3] Cao W, Li J, Chen H, Xue J. J Photonics Energy 2014;4(1):040990.
[4] Chen X, Xie Q, Li J. Ceram 2020;46(2):2309–16.
[5] Chen Y. Mater Sci Eng 2018;423:012170.
[6] Li J, Yang D, Zhu X, Sun H, Gao X, Wangyang P, et al. J Sol-Gel Sci Technol 2017;82:563–8.
[7] Talu S, Bramowicz M, Kulesza S, Solaymani S, Ghaderi A, Dejam L, et al. Superlattices Microst 2016;93:109–21.
[8] Dalouji V, Ebrahimi P, Binaei N, Tanhaee E, Nezafat NB, Dejam L, et al. J Supercond Nov Magn 2019;32:1319–26.
[9] Dejam L, Solaymani S, Achour A, Stach S, Talu S, Nezafat NB, et al. Chem Phys Lett 2019;719:78–90.
[10] Li J, Zhu X, Xie Q, Yang D. Ceram 2019;45(3):3871–7.
[11] Dhara S, Giri PK. Thin Solid Films 2012;520:5000–6.
[12] Zhang ZH, Ye ZZ, Ma DW, Zhu LP, Zhou T, Zhao BH, et al. Mater Lett 2005;59:2732.
[13] Yuan GD, Zhang WJ, Jie JS, Fan X, Tang JX, Shafiq I, et al. Adv Mater 2008;20:168.
[14] Solaymani S, Ghaderi A, Dejam L, Garczyk Z, Sapota W, Stach S, et al. Int J Hydrog Energy 2017;42(20):14205–19.
[15] Pathak TK, Kumar V, Prakash J, Purohit LP, Swart HC, Kroon RE. Sens Actuators, A 2016;247:475–81.
[16] Kampylafka V, Kostopoulos A, Modreanu M, Schmidt M, Gagaoudakis E, Tsagaraki K, et al. J Materiomics 2019;5(3):428–35.
[17] Dejam L, Shokri AA, Nazari HH, Elahi SM. J Mater Sci: Mater Electron 2017;28:9378–86.
[18] Shokri A, Dejam L. Int Nano Lett 2019;9:161–8.
[19] Roudbari A, Dalouji V, Solaymani S, Nezafat NB, Rezaee S. Int J Thermophys 2019;40:75.
[20] Nezafat NB, Ghoranneviss M, Elahi SM, Shafiekhani A, Ghorannevis Z, Solaymani S. Microsc Res Tech 2019;82(11):1884–90.
[21] Nezafat NB, Ghoranneviss M, Elahi SM, Shafiekhani A, Ghorannevis Z, Solaymani S. Int Nano Lett 2019;9(4):311–5.
[22] Fattahi M, Nezafat NB, Talu S, Solaymani S, Ghoranneviss M, Elahi SM, et al. J Alloys Compd 2020;831:154763.
[23] Upadhyay GK, Kumar V, Purohit LP. J Alloys Compd 2021;856:157453.
[24] Viezbicke BD, Patel S, Davis BE, Birnie D. Phys Status Solidi B 2015;252(8):1700–10.
[25] Dejam L, Elahi SM, Nazari HH, Elahi H, Solaymani S, Ghaderi A. J Mater Sci: Mater Electron 2016;27(1):685–96.
[26] Ilkhani M, Dejam L. J Mater Sci: Mater Electron 2021. https://doi.org/10.1007/s10854-020-05092-x.
[27] Hossain MS, Kabir H, Rahman MM, Hasan K, Bashar MS, Rahman M, et al. Appl Surf Sci 2016;392:854–62.
[28] Lim WF, Quah HJ, Hassan Z, Radzali R, Zainal N, Yam FK. J Alloys Compd 2015;649:337–47.
[29] Arslan YM. Opt Mater 2004;27:29–37.
[30] Joseph B, Manoj PK, Vaidyan VK. Ceram Int 2006;32:487–93.
[31] Hassanien AS, AklJournal AA. J Alloys Compd 2015;648:280–90.
[32] Talu S. Micro and nanoscale characterization of three dimensional surfaces. Cluj-Napoca, Romania: Basics and applications. Napoca Star Publishing House; 2015.
[33] Sobola D, Talu S, Solaymani S, Grmela L. Microsc Res Tech 2017;80(12):1328–36.
[34] Talu S, Achour A, Solaymani S, Nikpasand K, Dalouji V, Sari A, et al. Microsc Res Tech 2020;83:457–63.
[35] Zare M, Solaymani S, Shafiekhani A, Kulesza S, Talu S, Bramowicz M. Sci Rep 2018;8:10870.
[36] Stach S, Sapota W, Talu S, Ahmadpourian A, Luna C, Ghobadi N, et al. 3D Surface stereometry studies of sputtered TiN thin films obtained at different substrate temperatures. J Mater Sci Mater Electron 2017;28(2):2113–22.
[37] Mahmoodi A, Solaymani S, Amini M, Nezafat NB, Ghoranneviss M. Silicon 2018;10(4):1427–31.
[38] Mozaffari N, Solaymani S, Achour A, Kulesza S, Bramowicz M, Nezafat NB, et al. J Phys Chem C 2020;124(6):3692–701.
[39] Solaymani S, Kulesza S, Nezafat NB, Shafiekhani A, Talu S, Dalouji V, et al. Ind Eng Chem Res 2020;59(52):22520–32.
[40] Mwema FM, Akinlabi ET, Oladijo OP, Fatoba OS, Akinlabi SA, Talu S. Advances in manufacturing analysis: fractal theory in modern manufacturing. Woodhead Publishing Reviews: Mechanical Engineering Series, USA 2020;1(2):13–39. https://doi.org/10.1016/B978-0-12-819496-6.00002-6.
[41] Talu S, Bramowicz M, Kulesza S, Shafiekhani A, Ghaderi A, Mashayekhi F, Solaymani S. Ind Eng Chem Res 2015;54(33):8212–8.
[42] Talu S, Bramowicz M, Kulesza S, Dalouji V, Solaymani S, Valedbagi S. Fractal features of carbon–nickel composite thin films. Microsc Res Tech 2016;79(12):1208–13.
[43] Solaymani S, Yadav RP, Talu S, Achour A, Rezaee S, Nezafat NB. Averaged power spectrum density, fractal and multifractal spectra of Au nanoparticles deposited onto annealed TiO_2 thin films. Opt Quantum Electron 2020;52:491.
[44] Talu S, Stach S, Ghodselahi T, Ghaderi A, Solaymani S, Boochani A, et al. Chem B 2015;119(17):5662–70.
[45] Mountains Map® 8 Premium Software (Digital Surf, Besançon, France). Available from: http://www.digitalsurf.fr (last accessed July 27th, 2021).
[46] ISO 25178-2: 2012, Geometrical product specifications (GPS) - Surface texture: Areal - Part 2: Terms, definitions and surface texture parameters. Available from: http://www.iso.org (last accessed July 27th, 2021).